ROYAL SOCIETY
OF CHEMISTRY

PAPER

Check for updates

A facile approach to synthesize CdS–attapulgite as a photocatalyst for reduction reactions in water†

Ruixiao Ma,[ab] Liyan Xie,[b] Yixuan Huang,[a] Kangji Zhuo,[a] Juan Xu[a] and Yanhui Zhang [ID] *[ab]

At room temperature, a facile approach has been utilized for preparing novel CdS–attapulgite (CdS–ATP) composites and the composites were applied in photocatalytic reduction of p-nitrophenol and Cr(VI). The effect of ATP on the photocatalytic activity of the CdS–ATP composites were studied by controlling the mass ratio of attapulgite. The results showed that the CdS–20%ATP composite has an excellent photocatalytic activity. In order to figure out the key to improve the photocatalytic efficiency, the prepared composites were characterized by Brunauer–Emmett–Teller (BET) specific surface area, UV-vis diffuse reflectance spectroscopy (DRS) and electrochemical impedance spectroscopy (EIS). The superior photocatalytic performance of the CdS–20%ATP composite can be ascribed to the existence of the ATP which can fix the CdS and prevent agglomeration. The interaction between ATP and CdS in the composites facilitates the electron transfer and also promoted their photocatalytic performance. This work provides us with some significant guidance in the development of CdS–ATP composite photocatalysts.

Introduction

In a fast-developing society, more and more unpurified water enters into soil and groundwater, which not only has imperiled animals and plants but also human health due to the highly toxic, powerfully cancerogenic, and nonbiodegradable ingredients. The pollutants (*e.g.*, organic molecules, petroleum, and heavy metal ions) being intemperately discharged to the water has become a top environmental issue.[1–7] For example, p-nitrophenol (p-NP) is known as one of the pernicious contaminants among the organic pollutants. It is a menace to organisms at lower concentrations owing to its toxicity, carcinogenic, and mutagenic properties.[8,9] Physical, chemical and microbial methods have been extensively studied in the application of how to reduce it effectively.[10–18] In the previously reported

[a]*College of Chemistry, Chemical Engineering and Environment, Fujian Province Key Laboratory of Morden Analytical Science and Separation Technology, Minnan Normal University, Zhangzhou, 363000, P. R. China. E-mail: zhangyh@mnnu.edu.cn; Tel: +86 596 2591445*

[b]*Fujian Province Key Laboratory of Ecology-Toxicological Effect & Control for Emerging Contaminants, Putian University, Putian, 351100, P. R. China*

† Electronic supplementary information (ESI) available: Mg 1s, Al 2p, Si 2p and O 1s XPS spectra of CdS–20%ATP and ATP; The UV-visible absorption spectra of p-NP without ammonium formate by blank-CdS and CdS–20%ATP; the UV-visible absorption spectra of Cr(VI) when pH = 3 with CdS–20%ATP as catalyst; the photocatalytic reduction of p-NP when pH = 3 with CdS–20%ATP; N₂ adsorption–desorption isotherms of the ATP, blank-CdS, and CdS–20%ATP; the image of normalized K_a/S_{BET} of the blank-CdS, CdS–10%ATP, CdS–20%ATP and CdS–30%ATP; XRD patterns of CdS–20%ATP 4th run. See DOI: 10.1039/d1ra04530j

literature, the NaBH₄ system is mainly used for the reduction of p-NP in chemical methods, especially. However, this method has been widely and deeply studied, so it is of great significance to find a more convenient and feasible chemical method to reduce p-NP.[19,20] In addition, as a typical heavy metal pollutant, Cr(VI) often exists in the wastewater of printing and dyeing, electroplating, leather and metallurgy, which can cause great harm to humans through migration and bioaccumulation.[21,22] A series of technical methods such as adsorption, chemical leaching, ion exchange, precipitation, biological methods, and photocatalysis have been used to reduce the Cr(VI).[21,23–31] However, it is not easy to find a universal reduction technology, and we still need to make continuous efforts.

Hence, it is urgent to enrich advanced materials and develop versatile technologies for environmental remediation.[3,32,33] As a chalcogenide photocatalyst, CdS has attracted much interest because of its narrow band gap, high light harvesting and excellent catalytic properties.[34–36] However, the limitations of the high recombination rate of photogenerated electron–hole pairs, photocorrosion problems, and easy agglomeration of CdS hinder its further application in photocatalysis.[34,37–39] Therefore, many efforts have been made to optimize the properties of CdS such as the materials hybridization and element doping.[35,40,41]

Natural attapulgite (ATP) may be used as a perfect support material to hybridize with CdS because of the abundant reserves, attractive price, and special structure. And the ideal formula of the ATP is $Al_2Mg_2Si_8O_{20}(OH)_2(OH_2)_4 \cdot 4H_2O$. The adsorption, carrier and catalytic properties of ATP make it a promising catalyst in sewage disposal.[42–44] In the CdS–ATP

composites, ATP may not only play a role in fixing and avoiding agglomeration, but also can reduce light corrosion and improve light tolerance. In addition, as an ideal photocatalytic carrier material, ATP can also provide many microreaction sites for photocatalytic reaction.[45,46] Furthermore, the mesopores of ATP also could play the role of facilitating the mass transport in CdS–ATP composites, which may improve the photocatalytic performance in reduction reaction.[47,48] If CdS–ATP composites could be successfully compounded, the limitations of CdS can be overcome, making it more targeted in the application of photocatalysis. However, in the photocatalytic treatment of sewage, there is no research on ATP and CdS–ATP composites as photocatalysts. Thus, the application of ATP and CdS–ATP composites in photocatalysis needs to be pioneered and further explored.

Herein, the CdS–ATP composites are used for the photocatalytic reduction of p-NP and Cr(vi), which lays a foundation for the further development of CdS–ATP composites in photocatalysis. The effects of photocatalytic reduction efficiency were investigated by adjusting the mass ratio of the ATP. It was found that the photocatalytic efficiency of CdS–20%ATP composite has the most excellent efficiency under the premise of many microreaction sites that are provided by ATP. It can be attributed to not only the weakened photocorrosion but also the enhanced electron transfer by a series of performance analysis.

Experimental section

Preparation

Reagents. Cadmium nitrate tetrahydrate ($Cd(NO_3)_2 \cdot 4H_2O$), sodium sulfide nonahydrate ($Na_2S \cdot 9H_2O$) and potassium dichromate ($K_2Cr_2O_7$) were provided by Xilong Scientific Co., Ltd (Guangdong, China). p-Nitrophenol ($C_6H_5NO_3$), p-aminophenol ($C_6H_6N_2O_2$) and ammonium formate (CH_5NO_2) were supplied by Macklin Biochemical Co., Ltd (Shanghai, China). Attapulgite was purchased from Xuyi (Jiangsu, China). All the reagents were AR (analytical reagent) grade in purity. Deionized water used in all the processes was from local sources.

Synthesis. (a) Synthesis of blank-CdS. Firstly, 3.08 g of $Cd(NO_3)_2 \cdot 4H_2O$ was dissolved into 50 mL deionized water to obtain solution A. Secondly, solution B was prepared by ultrasonically dispersing 2.88 g of $Na_2S \cdot 9H_2O$ in 50 mL deionized water. Thirdly, solution A was slowly added into solution B by using a constant pressure separating funnel and the mixture was stirred for 6 h at room temperature. Finally, the acquired blank-CdS was obtained by centrifugation after washing by deionized water and ethanol for several times and then dried at 60 °C in an oven. (b) Synthesis of CdS–ATP composites. The different mass ratio of CdS–ATP composites were prepared by the above method. The difference is that the solution A was obtained by 3.08 g of $Cd(NO_3)_2 \cdot 4H_2O$ and different quality g of ATP fully mixed in 50 mL deionized water. When the mass of ATP are 0.1607 g, 0.3612 g and 0.6197 g, the CdS–10%ATP, CdS–20%ATP and CdS–30%ATP composites can be obtained respectively.

Characterization

The crystalline structure of the samples was determined by the powder X-ray diffraction (XRD, Rigaku Ultima IV) with Cu Kα_1 radiation (40 kV, 40 mA, $\lambda = 1.5406$ Å) in a 2θ ranging from 5° to 80° at the scan rate of 8° per minute. The morphology and microscopic structure informations were acquired by the scanning electron microscopy (SEM, Hitachi S4800), the transmission electron microscopy (TEM, Tecnai G2 F20) and the Brunauer–Emmett–Teller (BET, Quadrasorb evoTM) specific surface area analysis. The Fourier-transform infrared spectroscopy (FT-IR, Nicolet iS 10) and X-ray photoelectron spectroscopy (XPS, Thermo ESCALAB 250XI) measurements were performed to detect the structure, surface elements and the binding energy. The optical properties of the photocatalysts were analyzed by UV-vis diffuse reflectance spectroscopy (DRS, UH4150) using a Cary-500 spectrophotometer over a wavelength range of 300–800 nm, which $BaSO_4$ was utilized as the internal reflectance standard. The UV-vis absorption spectra were analyzed on a Varian UV-vis spectrophotometer (UV-1600PC). The photoelectrochemical properties was analyzed by the electrochemical impedance spectroscopy (EIS, CHI-660D).

Photocatalytic measurements

The suspensions were irradiated by the 300 W Xe arc lamp (PLS-SXE 300, Beijing Perfectlight Co. Ltd) as the simulated solar light source, and the beaker is used as the reaction vessel. 0.1 g of the sample and 0.1 g of ammonium formate (as a sacrificial agent for photogenerated holes) were added in 120 mL of the p-NP solution (10 mg L^{-1}). After stirring 40 min for achieving adsorption–desorption equilibrium, the initial concentration C_0 was obtained before irradiation. Then the other samples concentration C were obtained in a time interval of 2 min under simulated sunlight. After the reaction, the supernatant fluid was obtained by centrifugation and analyzed with Mapada UV-1600PC UV-vis spectrophotometer. The changes in absorption spectrum at 400 nm correspond to the concentration changes, and were plotted with $(1 - C/C_0) \times 100$ used as the ordinate and the irradiation time used as the abscissa, then the photoreduction efficiency was obtained.

The photoreduction efficiency of Cr(vi) was obtained by substituting 40 mg L^{-1} Cr(vi) for 10 mg L^{-1} p-NP, 0.05 g of the sample without ammonium formate as a capture agent and the irradiation time interval was shortened from 2 min to 1 min. Plot the changes of C/C_0 of Cr(vi) at 373 nm as the ordinate and the irradiation time as the abscissa.

Results and discussion

The crystallographic structures of all the samples were elucidate by XRD analysis, and the typical XRD patterns were shown in Fig. 1. The diffraction peaks of blank-CdS, at $2\theta = 26.5°$, $44.0°$, and $52.1°$, could assigned to the (111), (220), and (311) crystallographic planes, respectively, which could matched with the hawleyite structure of CdS (JCPDS no. 10-0454).[49] And the distinct broad peaks suggests a lower crystallinity. In the spectrum of ATP, the peaks at $2\theta = 8.5°$, $19.8°$, $20.8°$, $24.1°$, $26.6°$ and
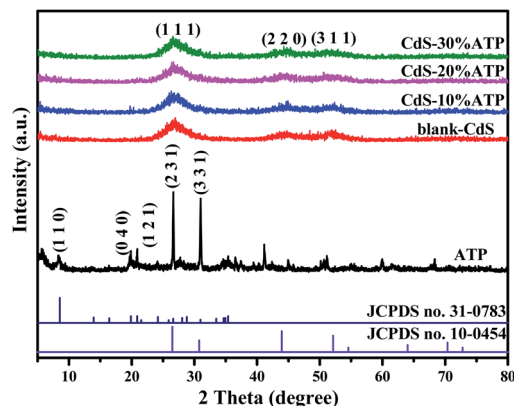
Fig. 1 The XRD patterns of blank-CdS, ATP, CdS−10%ATP, CdS−20% ATP and CdS−30%ATP.

30.9°, corresponding to the (110), (040), (121), (221), (231) and (331) crystal planes of palygorskite (JCPDS no. 31-0783), respectively.[50] However, after incorporation with CdS, the diffraction peaks for the ATP can not detected in CdS−ATP composites with different mass ratios. The reason may be that the content of the ATP is too low to be detected.

Furthermore, the FT-IR analysis was used to research the chemical composition of the obtained photocatalysts, and the FT-IR spectra of the blank-CdS, ATP, CdS−10%ATP, CdS−20% ATP, and CdS−30%ATP were shown in Fig. 2. In the FT-IR spectrum of blank-CdS, the wavenumber at 674, 1000 and 1380 cm^{-1} are attribute to the typical absorption of the Cd–S bond.[51] In the spectrum of ATP, on characteristic peaks at 800 and 1032 cm^{-1} can ascribed to the symmetric stretching vibration of Si–O and unsymmetric stretching vibration of Si–O–Si respectively.[43] And the broad-band between 3300 and 3500 cm^{-1} is due to the skeletal vibrations of O–H.[43] The major characteristic vibration peaks related to CdS and ATP can be clearly found in the composites, which implying that the structure of CdS remains intact after composited with ATP.

To further identify the chemical composition of the composites, the XPS analysis was applied to compared the different elements in ATP and CdS−20%ATP and the survey
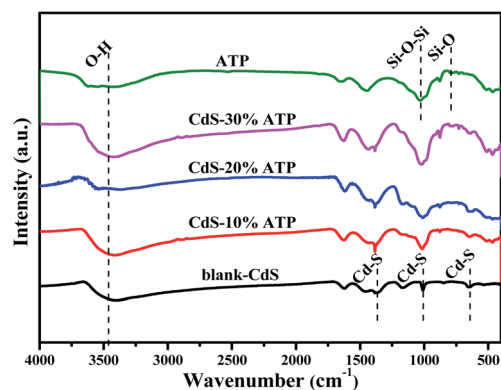
spectrum was shown in Fig. 3a. The peaks at binding energies about 405.5 eV and 412.2 eV could match well with the peaks of Cd 3d and the peaks about 175.1 eV could linked to S 2p in Fig. 3b and c.[35] In addition, the other detailed elements spectrum of CdS−20%ATP and ATP by XPS analysis were displayed in Fig. S1 (in the ESI†). In the spectrum of Mg 1s, Al 2p, Si 2p and O 1s Fig. S1,† the binding energy was slightly increased after compounding with CdS. Especially, the peaks of Al 2p has a peak separation, this may be due to the effect of CdS on the valence of Al in ATP. All the above phenomenon indirectly also proves that the CdS anchored on ATP surface successfully.

The morphologies of the photocatalysts were studied by SEM and TEM analysis. From Fig. 4a, it can be clearly seen that the rod-shaped structural of ATP, which is consistent with previous
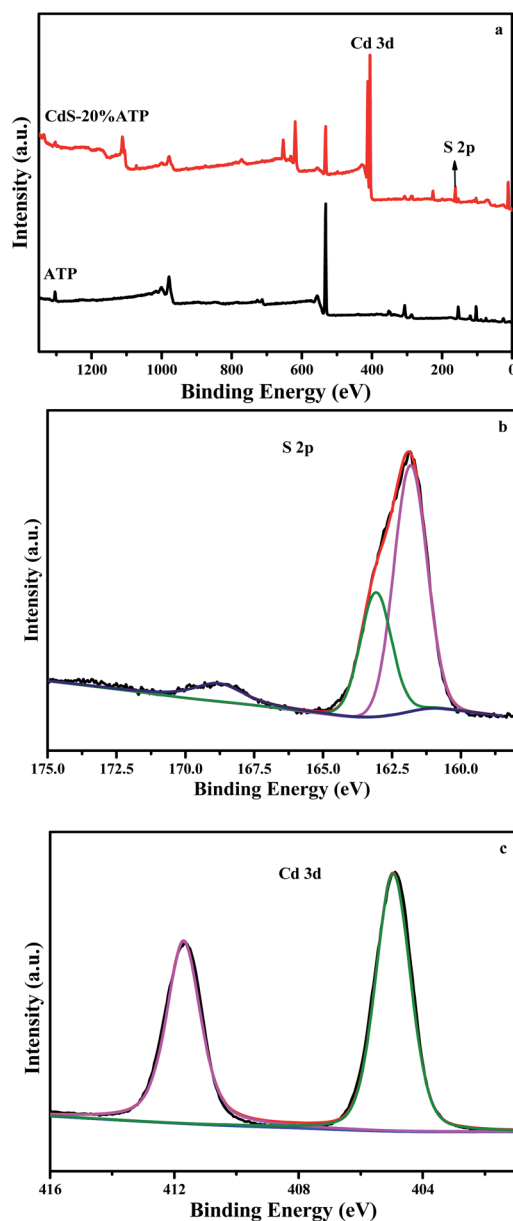

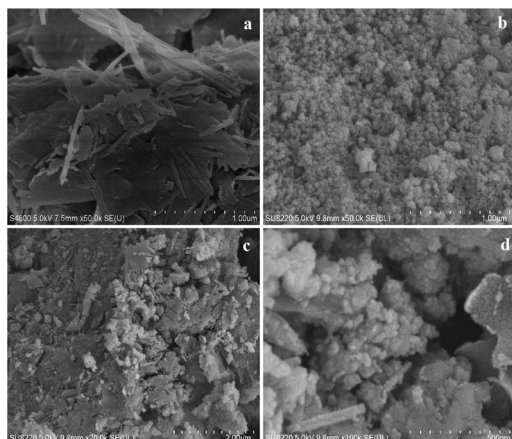Fig. 3 The XPS Survey of ATP and CdS−20%ATP (a), S 2p (b) and Cd 3d (c) XPS spectra of CdS−20%ATP.

Fig. 2 The FT-IR spectra of blank-CdS, ATP, CdS−10%ATP, CdS−20% ATP and CdS−30%ATP.

Fig. 4 The SEM of ATP (a), blank-CdS (b) and CdS−20%ATP (c and d).

Fig. 6 Photoreduction efficiency with 5% error bars of *p*-nitrophenol under simulated solar light irradiation for 10 min at room temperature.

reports.[52] The as-prepared blank-CdS were aggregated and the size of CdS nanoparticles is around 15 nm as depicted in Fig. 4b. It can be obviously seen that CdS nanoparticles successfully anchored on the surface of ATP support in CdS−20%ATP composite, as depicted in Fig. 4c and d. In addition, the TEM of CdS−20%ATP composite, shown in Fig. 5, further shows us the internal information of the CdS−20%ATP composite. In Fig. 5a, it can be seen that CdS has wrapped the ATP nanorods. The lattice fringes of CdS can be clearly seen in the Fig. 5b, and the spacing of the lattice fringe is 0.336 nm, which could be assigned to the (111) plane of CdS. In addition, the main elements of composite also can be detected from the EDS of CdS−20%ATP in Fig. 5c, and the main elements all be probed. There are three clear diffraction ring in the SAED of CdS−20% ATP, indicates the CdS crystallize well, and this also could be matched with the XRD patterns of CdS−20%ATP. From this results, we can extrapolate that the CdS−ATP composites was successfully prepared.

The photocatalytic activity of CdS−ATP composites were investigated *via* reduction of *p*-NP. Fig. 6 demonstrates
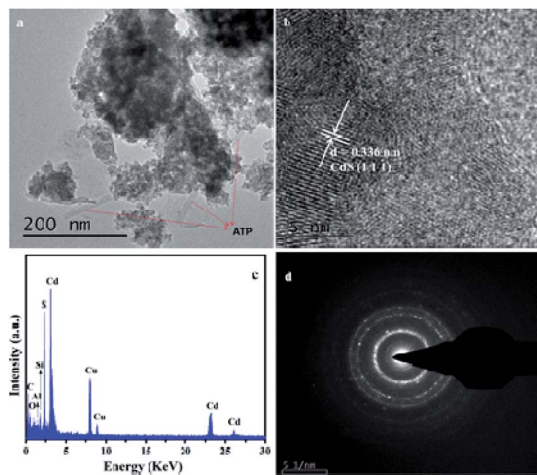

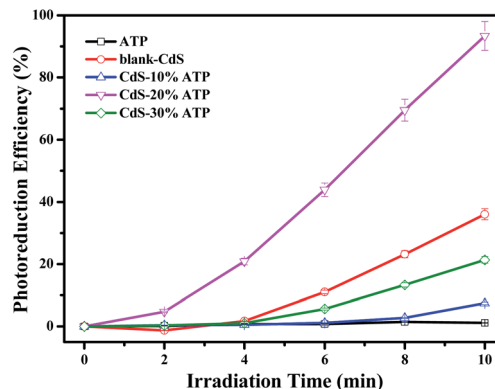Fig. 5 The TEM (a), HRTEM (b), EDS (c) and SAED (d) of CdS−20%ATP.

reduction ratio of *p*-NP when ammonium formate was used as sacrificial reagents under ambient conditions in water, where C_0 was the concentration of *p*-NP after adsorption for 40 min in the dark and C was the concentration of *p*-NP after irradiation.

As shown in Fig. 6, the concentrations of *p*-NP almost has no change when ATP is used as the photocatalyst, indicating that the ATP has no photocatalytic activity in photocatalytic reduction of *p*-NP. The blank-CdS exhibits a lower photocatalytic activity owing to the high recombination rate of photogenerated charge carriers.[37] Obviously, the CdS−20%ATP composites exhibits the optimal weight percent and has the highest reduction efficiency among the above samples in 10 min, giving a 2.6 times higher rate of *p*-NP reduction than blank-CdS. Indeed, we have also used the high performance liquid chromatograph (HPLC) to quantify the distribution of reactant and product, which confirms that the product is primarily dominated by *p*-AP with a high selectivity.

The blank experiment without ammonium formate was conducted in order to figure out the effect of ammonium formate during the photocatalytic reduction of *p*-NP. The UV-vis absorption characteristics of *p*-NP over blank-CdS and CdS−20% ATP was shown Fig. S2 (in the ESI†). As shown in Fig. S2,† it can be found that in the absence of ammonium formate, the absorbance of *p*-NP changes little, which indicates that ammonium formate is the key to photocatalytic reduction of *p*-NP.

The photocatalytic reduction of Cr(VI) has also been studied. Fig. 7a displays the photocatalytic efficiency of Cr(VI) with the samples of blank-CdS, ATP and different mass rations of CdS−ATP composites as photocatalysts. After adding the chromophoric reagent, the UV-Vis absorption spectrum indicates that the reduction product was mainly Cr(III) when the content of Cr(VI) decreases. Moreover, the pseudo-first-order relationship was revealed in Fig. 7b. The order of the kinetic rate constants are as follows: CdS−20%ATP (0.4467 min^{-1}) > CdS−10%ATP (0.3177 min^{-1}) > CdS−30%ATP (0.2435 min^{-1}) > blank-CdS (0.1903 min^{-1}) > ATP (0.0040 min^{-1}). As the mass ratio of ATP increases, the photocatalytic activities of CdS−ATP composites increase first, achieve a peak value at CdS−20%ATP, and then decrease. Which is consistent with the reduction of *p*-NP. The
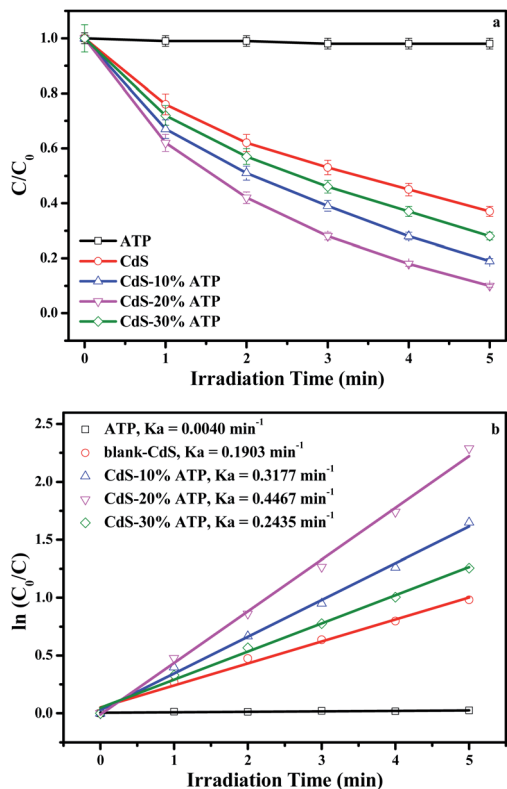
Fig. 7 Photocatalytic reduction of Cr(VI) under simulated solar light irradiation with 5% error bars (a) and the apparent rate constant (k_a) (b) in 5 min at room temperature.

Fig. 8 The UV-vis DRS of blank-CdS, ATP, CdS–10%ATP, CdS–20% ATP and CdS–30%ATP.

possible reasons are put forward as follows: under simulated solar light irradiation, with a low mass ratio (CdS–10%ATP), the photocatalytic activity of the CdS is improved by being mixed with ATP, which is beneficial to boost the light absorption in the visible and ultraviolet regions. Then, the photocatalytic activity of CdS–ATP composites can be enhanced with the increase in the ATP amount. After the maximum, the photocatalytic activity of CdS–ATP composites decreases with the increase of ATP (CdS–30%ATP). This could be due to excessive ATP that covers the active sites of CdS, which hinders the light absorption and electron transfer, thus, in turn inhibits the photocatalytic activity.

In order to explore the effect of pH on the reaction, we adjusted the pH to 3 for photocatalytic experiment under the same conditions. The UV-vis absorption spectrum of Cr(VI) was shown in Fig. S3 (in the ESI†). As the pictures depicted, the characteristic absorption peak of Cr(VI) at 373 nm disappeared. That reason may be that the Cr(VI) could convert to Cr(III) easily according to the formula: $Cr_2O_7^{2-} + H^+ \rightarrow 2Cr^{3+} + H_2O$.[53] When reduction of p-NP, the conversion was hindered when pH = 3 from Fig. S4 (in the ESI†). Because the acidic condition is not conducive to the deprotonation of p-NP.[19]

UV-vis DRS analysis was conducted in order to investigate the optical properties of all the samples. As illustrated in Fig. 8, in ultraviolet region all samples have strong absorption. The absorption edge of ATP is about 400 nm, means a weaker
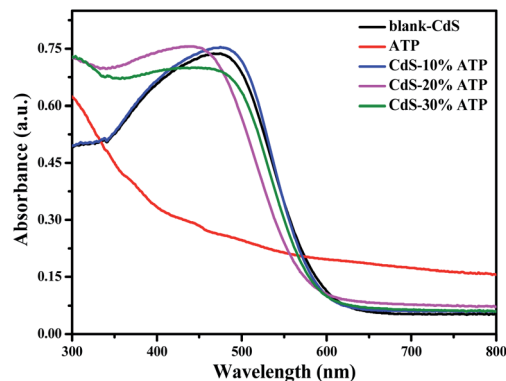
absorption in visible region. However, the absorption edge of blank-CdS is about 600 nm, suggesting an excellent light absorption in visible region. Compared with blank-CdS, the absorption edge of CdS–ATP composites have a slight blue shift, but it has a insignificant effect on the light absorption capacity. That is to say, the light absorption is not enhanced in CdS–ATP composites, thus, the light harvesting efficiency is not the main factor of the photocatalytic activity.

The N_2 adsorption–desorption experiments were carried out to get the Brunauer–Emmett–Teller (BET) specific surface area and the porous structure of ATP, blank-CdS and CdS–20%ATP. According to the IUPAC classification, as seen from Fig. S5 (in the ESI†), the N_2 adsorption–desorption isotherms of the ATP shows a type III adsorption–desorption isotherm with a H3 hysteresis loop indicating the presence of mesopores.[54] The blank-CdS and CdS–20%ATP composites both exhibit a type V adsorption–desorption isotherm which is similar to the type III. As depicted in Table 1, the surface area of CdS–20%ATP decreased little compared with the blank-CdS. As seen from Fig. S6 (in the ESI†), the normalized K_a/S_{BET} of all the photocatalysts, the CdS–20%ATP composites shows the largest K_a per m2, indicating the 20% of ATP is the optimal ratio in composites. That may be the effect of mesopores in CdS–ATP composites which could promote the mass transport rather than the specific surface area.[47,48] That may be why the CdS–20%ATP composites has the best catalytic efficiency though the surface area changes little.

In order to study the carrier separation of the photocatalyst, the photoelectrochemical properties of ATP, blank-CdS and

Table 1 Summary of surface area and pore size of the ATP, blank-CdS, CdS–10%ATP, CdS–20%ATP and CdS–30%ATP

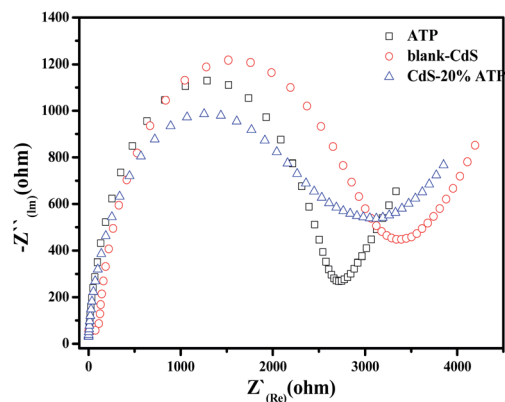| Sample	S_{BET} ($m^2 \ g^{-1}$)	Pore size (nm)
ATP	105	6.8
Blank-CdS	128	5.7
CdS–10%ATP	112	9.7
CdS–20%ATP	127	12.4
CdS–30%ATP	138	11.6

Fig. 9 Electrochemical impedance spectra (EIS) of blank-CdS, ATP and CdS–20%ATP.

CdS–20%ATP were evaluated by electrochemical impedance spectroscopy (EIS). It is worth noting that, compared with other samples, the introduction of ATP leads to distinctly decrease in the arc for CdS–20%ATP as seen in Fig. 9. This is favorable evidence that, on CdS–20%ATP, carrier transfer is more effective than other samples. Therefore, it is clear that CdS with rod-shaped crystal aggregates of ATP can promote the interfacial electron transport more efficiently than blank-CdS and ATP. And that's why CdS–20%ATP exhibits a higher efficiency in reduction of p-NP and Cr(VI) than blank-CdS.

To evaluate whether CdS–20%ATP was reusable as photo-catalysts, the recycled experiments for photoreduction of p-NP has been performed, and the results are shown in Fig. 10. During four successive cycles, there is no obvious photocatalytic activity loss in reduction of p-NP under the simulated sunlight irradiation, suggesting that CdS–20%ATP composites have an excellent stability for the photoreduction. In addition, we also investigated the crystal structure of XRD analysis of CdS–20% ATP composites after four successive cycles in reduction of Cr(VI), as depicted in Fig. S7 (in the ESI†). From the XRD pattern, there is no obviously change in the crystal structure of CdS–20% ATP composites after four cycles, which also indicating that the CdS–20%ATP is stable and light-resistant.
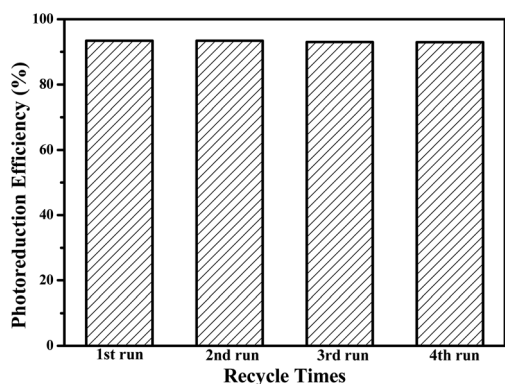

Fig. 10 Recycle testing of the photoreduction efficiency of CdS–20% ATP of p-NP under simulated solar light irradiation in water.
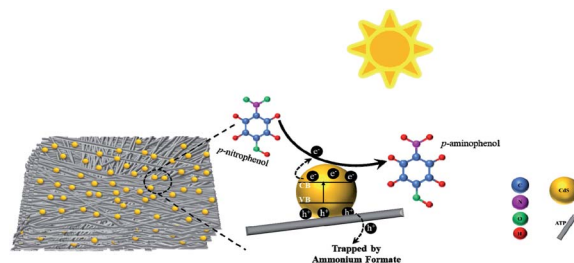

Fig. 11 Possible mechanism of photocatalytic reduction of p-NP under simulated solar light.

When the simulated solar light starts to irradiate, the electrons in the valence band of CdS are excited to transition to its conduction band and convert into photogenerated electrons.

The photogenerated holes remain in the valence band, correspondingly. Furthermore, due to the lower resistance of charge transfer in CdS–20%ATP composites, the lifetime of photogenerated carriers is effectively extended, which is very beneficial to photocatalytic reduction. The existence of meso-pores in CdS–20%ATP composites also could accelerate the mass transport during the reaction. In the reduction of p-NP, the photogenerated holes trapped by ammonium formate, and the photogenerated electrons worked on p-NP to turn into p-AP. In this reaction, the ammonium formate is pivotal for triggering the photoreduction because without the hole sacrificial agent the reaction is difficult to start. As for Cr(VI), the experiment can be carried out without sacrificing agent. Similar to typical photocatalytic reactions, the photogenerated electrons captured by Cr(VI), and then reduced into Cr(III).

Based on the above experiments and analysis, the probable photocatalytic reduction mechanism for CdS–20% ATP is proposed, as shown in Fig. 11 (Take reduction of p-NP as the example).

Conclusions

This work has developed the CdS–ATP composites through a facile method and applied them in photocatalytic reduction of p-NP and Cr(VI). From the photocatalytic data, the CdS–20%ATP composites exhibit a better photoreduction efficiency than blank-CdS and other CdS–ATP composites. The possible reasons are as follows: (1) there are many microreaction sites provided by ATP which could accelerate the adsorption of pollutants and promote the progress of photoreduction reac-tions, (2) the CdS particles have enhanced photocorrosion resistance because of being settled on the ATP support, (3) the lower impedance in CdS–20%ATP composites enhances the electron transport and prolongs the photogenerated carriers lifetime. And this is the main factor to improve the efficiency of photocatalytic reduction. Because of the breakthroughs in photocatalysis with CdS–ATP composites and the outstanding photoreduction efficiency in a short time, the CdS–ATP composites have a promising and bright future in the applica-tions of photocatalysis.

Conflicts of interest

There are no conflicts to declare.

Acknowledgements

Notes and references

1 P. Shao, S. Yu, X. Duan, L. Yang, H. Shi, L. Ding, J. Tian, L. Yang, X. Luo and S. Wang, *Environ. Sci. Technol.*, 2020, **54**, 8464–8472.

2 P. Shao, J. Tian, F. Yang, X. Duan, S. Gao, W. Shi, X. Luo, F. Cui, S. Luo and S. Wang, *Adv. Funct. Mater.*, 2018, **28**, 1705295.

3 F. Zhang, W. Liu, S. Zhou, L. Jiang, K. Wang, Y. Wei, A. Liu, W. Wei and S. Liu, *Anal. Chem.*, 2020, **92**, 7200–7208.

4 H. Zhou and Y. Zhang, *Phys. Chem. Chem. Phys.*, 2019, **21**, 21798–21805.

5 X. Chen, Z. Wu, D. Lai, M. Zheng, L. Xu, J. Huo, Z. Chen, B. Yuan and M.-L. Fu, *J. Mater. Chem. A*, 2020, **8**, 22645–22656.

6 P. Shao, D. Liang, L. Yang, H. Shi, Z. Xiong, L. Ding, X. Yin, K. Zhang and X. Luo, *J. Hazard. Mater.*, 2020, **387**, 121676.

7 H. Yu, P. Shao, L. Fang, J. Pei, L. Ding, S. G. Pavlostathis and X. Luo, *Chem. Eng. J.*, 2019, **359**, 176–185.

8 M. Shahriari, Z. Akhavan and G. Khayati, *J. Chem. Eng. Data*, 2020, **65**, 5101–5109.

9 X. Tian, X. Wang, Y. Nie, C. Yang and D. D. Dionysiou, *Environ. Sci. Technol.*, 2021, **55**, 2403–2410.

10 J. Kuntail, Y. Jain, M. Shukla and I. Sinha, *J. Mol. Liq.*, 2019, **288**, 111053.

11 B. Cui, J.-C. Gong, M.-H. Duan, Z.-X. Chang, L.-L. Su, W.-J. Liu and D.-L. Li, *J. Chem. Eng. Data*, 2016, **61**, 813–819.

12 M. Cheng, J. Jiang, J. Wang and J. Fan, *ACS Sustainable Chem. Eng.*, 2019, **7**, 8195–8205.

13 A. Bhattacharjee and M. Ahmaruzzaman, *RSC Adv.*, 2016, **6**, 41348–41363.

14 B. Zhang, X. Zhan, P. Zhao and Z. Li, *RSC Adv.*, 2015, **5**, 57640–57646.

15 Y. Huang, H. Lin and Y. Zhang, *J. Solid State Chem.*, 2020, **283**, 121150.

16 Y. Zhang, H. Guo, W. Weng and M.-L. Fu, *Phys. Chem. Chem. Phys.*, 2017, **19**, 31389–31398.

17 A. Das and A. Dey, *J. Environ. Chem. Eng.*, 2020, **8**, 103830.

18 D. Kalaimurugan, P. Sivasankar, K. Durairaj, M. Lakshmanamoorthy, S. A. Alharbi, S. A. A. Yousef, A. Chinnathambi and S. Venkatesan, *Saudi J. Biol. Sci.*, 2021, **28**, 833–839.

19 C. Huang, W. Ye, Q. Liu and X. Qiu, *ACS Appl. Mater. Interfaces*, 2014, **6**, 14469–14476.

20 Y. Huang, L. Xie, K. Zhuo, H. Zhou and Y. Zhang, *New J. Chem.*, 2021, **45**, 3120–3127.

21 W. Qu, D. He, Y. Guo, Y. Tang, J. Shang, L. Zhou, R. Zhu and R.-J. Song, *Ind. Eng. Chem. Res.*, 2019, **58**, 18508–18518.

22 J. Tang, J. He, T. Liu and X. Xin, *RSC Adv.*, 2017, **7**, 33385–33401.

23 S. Bae, Y. Sihn, D. Kyung, S. Yoon, T. Eom, U. Kaplan, H. Kim, T. Schäfer, S. Han and W. Lee, *Environ. Sci. Technol.*, 2018, **52**, 10647–10656.

24 Y. Zhao, H. Li, B. Li, Y. Lai, L. Zang and X. Tang, *Anal. Methods*, 2021, **13**, 1269–1277.

25 J. A. Korak, R. Huggins and M. Arias-Paic, *Water Res.*, 2017, **118**, 141–151.

26 Y. Xie, J. Lin, J. Liang, M. Li, Y. Fu, H. Wang, S. Tu and J. Li, *Chem. Eng. J.*, 2019, **378**, 122107.

27 W. Ma, M. Wang, Z. Chen, F. Meng, Z. Cheng, D. Tan, Y. Pan, S. Duan and J. Gao, *ACS Sustainable Chem. Eng.*, 2019, **7**, 6323–6334.

28 C. Dai, X. Zuo, B. Cao and Y. Hu, *Environ. Sci. Technol.*, 2016, **50**, 1741–1749.

29 K. V. G. Ravikumar, D. Kumar, G. Kumar, P. Mrudula, C. Natarajan and A. Mukherjee, *Ind. Eng. Chem. Res.*, 2016, **55**, 5973–5982.

30 Y. Feng, Q. Chen, M. Cao, N. Ling and J. Yao, *ACS Appl. Nano Mater.*, 2019, **2**, 5973–5980.

31 G. Zhao, Y. Sun, Y. Zhao, T. Wen, X. Wang, Z. Chen, G. Sheng, C. Chen and X. Wang, *Langmuir*, 2019, **35**, 276–283.

32 M. A. Suntsova and O. V. Dorofeeva, *J. Chem. Eng. Data*, 2016, **61**, 313–329.

33 Z.-B. Fang, T.-T. Liu, J. Liu, S. Jin, X.-P. Wu, X.-Q. Gong, K. Wang, Q. Yin, T.-F. Liu, R. Cao and H.-C. Zhou, *J. Am. Chem. Soc.*, 2020, **142**, 12515–12523.

34 J. Lv, J. Zhang, J. Liu, Z. Li, K. Dai and C. Liang, *ACS Sustainable Chem. Eng.*, 2018, **6**, 696–706.

35 J. Wang, Y. Pan, L. Jiang, M. Liu, F. Liu, M. Jia, J. Li and Y. Lai, *ACS Appl. Mater. Interfaces*, 2019, **11**, 37541–37549.

36 L. Li, X. Li, Z. Cheng, J. Bi, S. Liang, Z. Zhang, Y. Yu and L. Wu, *Dalton Trans.*, 2018, **47**, 7077–7082.

37 L. Zou, H. Wang, G. Yuan and X. Wang, *ACS Appl. Nano Mater.*, 2018, **1**, 831–838.

38 J.-X. Lv, Z.-M. Zhang, J. Wang, X.-L. Lu, W. Zhang and T.-B. Lu, *ACS Appl. Mater. Interfaces*, 2019, **11**, 2655–2661.

39 Y. Shi, H. Wang, Z. Wang, T. Wu, Y. Song, B. Guo and L. Wu, *J. Mater. Chem. A*, 2020, **8**, 18755–18766.

40 K. Li, R. Chen, S.-L. Li, S.-L. Xie, L.-Z. Dong, Z.-H. Kang, J.-C. Bao and Y.-Q. Lan, *ACS Appl. Mater. Interfaces*, 2016, **8**, 14535–14541.

41 L. Zhang, Q. Zhang and Y. Luo, *J. Phys. Chem. Lett.*, 2017, **8**, 5680–5686.

42 X. Mao, Y. Duan and C. Wang, *J. Chem. Eng. Data*, 2018, **63**, 4241–4247.

43 J. Liu, J. Liu, J. Zhong, J. Shen and S. Ren, *Energy Fuels*, 2021, **35**, 5172–5180.

44 X.-Y. Xie, X.-Y. Qian, S.-C. Qi, J.-K. Wu, X.-Q. Liu and L.-B. Sun, *ACS Sustainable Chem. Eng.*, 2018, **6**, 13217–13225.

45 Z. Zhu, Y. Yu, H. Dong, Z. Liu, C. Li, P. Huo and Y. Yan, *ACS Sustainable Chem. Eng.*, 2017, **5**, 10614–10623.

46 X. Liu, Y. Xue, Y. Lei, F. Wang and S. Min, *ACS Appl. Nano Mater.*, 2018, **1**, 6493–6501.

47 Y. Xing, Y. Wang, C. Zhou, S. Zhang and B. Fang, *ACS Appl. Mater. Interfaces*, 2014, **6**, 2561–2567.

48 B. Fang, S.-Q. Fan, J. H. Ki, M.-S. Kim, M. Kim, N. K. Chaudhari, J. Ko and J.-S. Yu, *Langmuir*, 2010, **26**, 11238–11243.

49 C. Pang, L. Gao, A. V. Singh, H. Chen, M. K. Bowman, N. Bao, L. Shen and A. Gupta, *Chem. Mater.*, 2018, **30**, 1701–1709.

50 H. Guo, H. Zhang, Q. Li, F. Peng, L. Xiong, C. Wang, A. Hu, S. Yao and X. Chen, *Energy Fuels*, 2020, **34**, 9463–9472.

51 W. Zhong, X. Wu, P. Wang, J. Fan and H. Yu, *ACS Sustainable Chem. Eng.*, 2020, **8**, 543–551.

52 H. Chen, W. Wu, C. Liang and X. Wu, *Energy Fuels*, 2016, **30**, 4150–4158.

53 Y. T. He and S. J. Traina, *Environ. Sci. Technol.*, 2005, **39**, 4499–4504.

54 S. Lowell, J. E. Shields, M. A. Thomas and M. Thommes, *Characterization of Porous Solids and Powders: Surface Area, Pore Size and Density*, Kluwer Academic Publishers, Dordrecht, The Netherlands, 2004.